ADVANCED MATERIALS
www.advmat.de

Linearly Interlinked Fe-N_x-Fe Single Atoms Catalyze High-Rate Sodium-Sulfur Batteries

Jiufeng Ruan, Yao-Jie Lei, Yameng Fan, Marcela Chaki Borras, Zhouxin Luo, Zichao Yan, Bernt Johannessen, Qinfen Gu, Konstantin Konstantinov, Wei Kong Pang, Wenping Sun, Jia-Zhao Wang, Hua-Kun Liu, Wei-Hong Lai,* Yun-Xiao Wang,* and Shi-Xue Dou*

Linearly interlinked single atoms offer unprecedented physiochemical properties, but their synthesis for practical applications still poses significant challenges. Herein, linearly interlinked iron single-atom catalysts that are loaded onto interconnected carbon channels as cathodic sulfur hosts for room-temperature sodium-sulfur batteries are presented. The interlinked iron single-atom exhibits unique metallic iron bonds that facilitate the transfer of electrons to the sulfur cathode, thereby accelerating the reaction kinetics. Additionally, the columnated and interlinked carbon channels ensure rapid Na^+ diffusion kinetics to support high-rate battery reactions. By combining the iron atomic chains and the topological carbon channels, the resulting sulfur cathodes demonstrate effective high-rate conversion performance while maintaining excellent stability. Remarkably, even after 5000 cycles at a current density of 10 A g^{-1}, the Na-S battery retains a capacity of 325 mAh g^{-1}. This work can open a new avenue in the design of catalysts and carbon ionic channels, paving the way to achieve sustainable and high-performance energy devices.

1. Introduction

The rapid growth of the hybrid electric vehicle and portable electronic device industries necessitates the development of fast-charging devices that can meet the urgent demand for sustainable energy systems.[1] Room temperature sodium-sulfur (RT/Na-S) rechargeable batteries have garnered significant attention as a cost-effective energy storage system with high energy density.[2] Despite notable advances in the design of state-of-the-art cathode materials, achieving dynamically stable RT/Na-S batteries still poses challenges for practical applications. In the multi-step sulfur reduction reaction, the sodium polysulfide intermediate (Na_2S_n, $4 \leq n \leq 8$) undergoes conversion to Na_2S_2/Na_2S at a lower voltage platform with increased activation energy. This conversion involves a rate-determining step that plays a critical role in the slow kinetics of sodium-sulfur batteries.[3] Moreover, the susceptibility of Na_2S_n to nucleophilic reactions with lipid electrolytes, as well as its propensity to dissolve readily in ether electrolytes, can result in a reduction in both battery capacity and stability.[4] To address these challenges, researchers have developed a variety of advanced catalysts to improve the reaction kinetics of S cathodes.

Catalysts primarily enhance the performance of sulfur cathodes by facilitating electron transfer and surface adsorption.[5]

J. Ruan, Y. Fan, M. C. Borras, K. Konstantinov, W. K. Pang, J.-Z. Wang, W.-H. Lai, Y.-X. Wang
Institute for Superconducting & Electronic Materials
University of Wollongong
Innovation Campus
Wollongong, New South Wales 2500, Australia
E-mail: wkpang@uow.edu.au; weihongl@uow.edu.au; yunxiao@uow.edu.au

Y.-J. Lei
Centre for Clean Energy Technology
University of Technology Sydney
Sydney, New South Wales 2007, Australia

Z. Luo, W. Sun
School of Materials Science and Engineering
Zhejiang University
Hangzhou, Zhejiang 310058, China

Z. Yan
State Key Laboratory of Chemo/Biosensing and Chemometrics
College of Chemistry and Chemical Engineering
Hunan University
Changsha, Hunan 410082, China

B. Johannessen, Q. Gu
Australian Synchrotron
800 Blackburn Road, Clayton, VIC 3168, Australia

H.-K. Liu, Y.-X. Wang, S.-X. Dou
Institute of Energy Material Science
University of Shanghai for Science and Technology
Shanghai 200093, China

The ORCID identification number(s) for the author(s) of this article can be found under https://doi.org/10.1002/adma.202312207

DOI: 10.1002/adma.202312207

Low-valence metallic particles or compounds efficiently transfer electrons to sulfur or sodium sulfide species, thereby accelerating their conversion.[5a,b,6] The limited surface area of large particles, however, demonstrates insufficient adsorption of unstable long chain polysulfides, resulting in a decline in capacity.[5a,7] Transition metal single-atom catalysts offer numerous active sites and are capable of immobilizing polysulfides. Nonetheless, the coordination with nitrogen decreases the electron transport capacity of single metal atoms.[8] Thus, future catalyst development should focus on enhancing the electron-transfer capability by building metallic surfaces while maximizing the number of active sites for room-temperature sodium-sulfur batteries. Single-atom-width metallic 1D catalysts are important options; However, their synthesis still poses great challenges and has not been reported for battery applications yet.

Moreover, efficient electron transport in rechargeable batteries necessitates the diffusion of Na^+ ions to achieve electrostatic neutrality. Consequently, the establishment of high-speed Na^+ migration pathways is crucial to overcome the sluggish reaction rates of sodium-sulfur batteries.[1a,3a,9] Meso-microporous carbon materials are commonly used for hosting sulfur cathodes, although the evolution of the carbon structure during the sintering process complicates matters. This complexity can create inhospitable spaces for Na^+ ion diffusion. Highly graphitic carbon has narrower interlayer spaces, hindering the movement of Na^+ ions. Conversely, carbon materials with low graphitization levels possess a discontinuous structure, which is detrimental to the transportation of both electrons and Na^+ ions.[10] Hence, it is vital to design advanced Na^+ ion channels that facilitate dynamic ion kinetics to improve the sluggish kinetics of sodium-sulfur batteries.

In this study, a high-performance sulfur cathode is presented for constructing linearly interlinked iron single-atom catalysts (IFeSACs) in an interconnected columnated carbon channel. The linear iron atomic chains act as electron reservoirs, providing extra electrons to accelerate the conversion of sulfur and sodium sulfide species. The columnated carbon channels offer interlinked pathways for the rapid diffusion of sodium ions, ensuring efficient electrochemical reactions at a high rate. With the iron atomic chains, the immobilization of polysulfides within the carbon structure prevents the shuttle effect, resulting in improved cycling stability. Advanced techniques have been utilized to reveal the working mechanism of our proposed structure. Overall, the integration of iron atomic chains with ion-hospitable carbon channels represents a promising strategy for the development of dynamic Na-S batteries.

2. Results and Discussion

2.1. Construction of Fe-N_x-Fe IFeSACs in Columnated and Interconnected Carbon Channels

In this work, pre-graphitic nitrogen-doped carbon was utilized to host iron atomic chains (Refer to the experimental section for more details). The pre-graphitic carbon has a slight amount of graphitic interspace, which enables the embedding of iron atoms. On the other hand, these nitrogen sites at the edge of these graphitic layers can work as bonding sources to immobilize the Fe atoms during the subsequent graphitization process. When the carbon host gradually develops its graphitic crystalline structure, the nitrogen-doped graphitic layers shape these Fe atoms to create a chain-like formation. Three graphitization temperatures of 600/700/800 °C have been investigated, and the corresponding samples are denoted as Fe/NC/600, Fe/NC/700, and Fe/NC/800. All three samples feature a similar Fe loading mass of 5 wt% in an even dodecahedral morphology after the sintering process (Figures S1 and S2, Supporting Information). As presented in **Figure 1**a, the high-resolution high-angle annular dark-field scanning transmission electron microscope (HAADF-STEM) image of Fe/NC/700 showcases interlinked Fe single atoms with a linear shape. It clearly demonstrates that the IFeSACs, resembling a chain, have an exceptionally narrow width of just one atom. Also, the typical HAADF-STEM image of Fe/NC/700 shows that these interconnected atom spots are evenly distributed in a porous carbon framework (Figure 1b). The enlarged image of the inverse fast Fourier transform (FFT) clearly highlights the chain-like structure formed by the interconnected Fe atoms on Fe/NC/700 (Figure 1c). The 3D electron intensity image of the selected Fe confirms that the atoms with higher electron intensity are the Fe atoms (Figure 1d). Controlling the carbonization temperature is essential for achieving this structure. Although the energy-dispersive spectroscopy (EDS) mappings of Fe/NC/600, Fe/NC/700, and Fe/NC/800 further indicate a uniform distribution of Fe within the carbon host, respectively (Figures S3–S5, Supporting Information), our findings suggest that Fe/NC/600 initially has a higher proportion of isolated single atom, while Fe/NC/800 forms agglomerated Fe atoms in clusters instead of particles (Figure 1e). Further, X-ray diffraction (XRD) patterns are characterized by the low intensity of the broad peaks at ≈24°, which can be indexed to the fingerprints of graphite reflections (Figure S6, Supporting Information). Additionally, it is obvious no diffraction peaks corresponding crystalline species of Fe, suggesting the Fe phase exists in the form of isolated single atomic Fe. Based on HAADF-STEM images, we found that ≈70% of Fe atoms in sample S@Fe/NC/700 form a linear chain structure (Figures S7 and S8, Supporting Information). In contrast, 80% atoms in the sample Fe/NC/600 are single atoms, while sample Fe/NC/800 has 56% atoms forming clusters. This implies that the Fe atoms gradually aggregate as the temperature increases. To further investigate the structural changes of Fe under different sintering temperatures, synchrotron-based X-ray absorption spectroscopy (XAS) results were employed. The X-ray absorption near-edge structure (XANES) spectra show that the valence state of Fe gradually decreases with increasing temperature, indicating a more metallic status (Figure S9, Supporting Information).[11] Additionally, X-ray photoelectron spectroscopy (XPS) in Figure S10 (Supporting Information) shows that the Fe 2P spectrum can be divided into the positively charged Fe species (≈709.5 eV and 712.7 eV for Fe^{2+} and Fe^{3+}), and with the increase in sintering temperature, the proportion of low-valence state Fe^{2+} gradually increases, which is aligning with the XAS result. The reason for the decreased valence of Fe/NC/700 is mainly because of the formation of Fe-Fe bonds, which is also consistent with the measured atomic distance. The chain-like IFeSACs have a bond length ranging from 2.34 Å to 2.57 Å, which is well matched with the theoretical Fe-Fe bond length of 2.48 Å (Figure S11, Supporting Information). Also, the Fourier-transformed-extended X-ray absorption fine structure (EXAFS) spectra observe an Fe-Fe

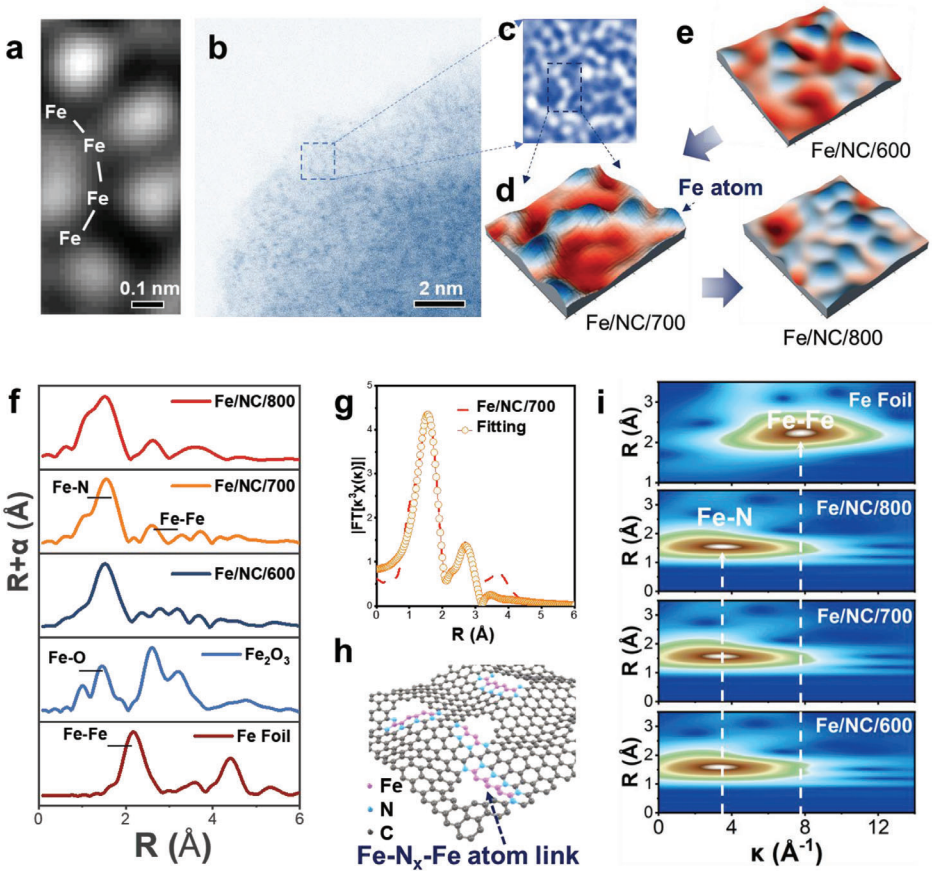

Figure 1. a) Inverse FFT pattern of the high-resolution HAADF-STEM image of Fe/NC/700. b) Typical HAADF-STEM image of Fe/NC/700. c) Inverse FFT pattern of the selected rectangular area in (a) and its corresponding 3D electron intensity profile (d). e) Selected 3D electron intensity profiles of Fe/NC/600 and Fe/NC/800. f) Normalized FT-EXAFS curves of Fe/NC/600, Fe/NC/700, Fe/NC/800, Fe_2O_3, and Fe foil in R-space. g) Corresponding Fe K-edge k^3-weighted FT-EXAFS fitting curve of Fe/NC/700 in R space. Data ranges: $3.0 \leq k \leq 10.3$ Å^{-1}, $1.0 \leq R \leq 3.0$ Å. h) Illustration of the fitted structure of IFeSACs. i) The WT plots for Fe element of Fe/NC/600, Fe/NC/700, Fe/NC/800, and Fe foil by using k^2 space.

peak at ≈2.6 Å in the Fe/NC/700 sample, although it becomes stronger at the temperature of 800 °C (Figure 1f). The absence of the Fe-Fe peak in Fe/NC/600 can be attributed to the formation of Fe single atoms. The EXAFS fitting further confirms that the Fe/NC/700 demonstrates Fe-N path in its first shell and Fe-N-Fe path in the second shell (Figure 1g, Table S1, Supporting Information). This result depicts an IFeSAC structure that has been formed in the Fe/NC/700 (Figure 1h). Moreover, the coordination number of Fe/NC/600, Fe/NC/700, and Fe/NC/800 increases as the temperature rises, which aligns well with the STEM observations (Figures S12, S13 and Table S1, Supporting Information). The wavelength transformation (WT) plots also show an increased intensity assignable to Fe-Fe path (≈7.9 Å) besides the main intensity maximum at ≈3.8 Å, further confirming the existence of Fe-Fe bonding (Figure 1i). Based on the analysis and experimental results above, we can conclude that the Fe/NC/700 sample forms 1D IFeSACs. The formation of this atomic chain structure is closely related to the temperature of the graphitic process. Additionally, the synergistic graphitic process of the carbon host plays a crucial role in the evolution of the Fe structure, as it transforms from a highly amorphous structure to a mild graphitic structure, shaping the agglomerated Fe atoms into a chain-like structure.

More importantly, the increase of sintering temperature induces changes of carbon structures, which are crucial for the reformation of Na^+ ion channels. As shown in **Figure 2**a, the carbon fringes continuously narrow the interlayer spacing from 0.407 nm to 0.347 nm with increasing temperature from 600 to 800 °C. The reason is that raising the carbonization temperature diminishes the disarray in the carbon structure and leads to the formation of larger, interconnected pseudographitic clusters in the Fe/NC/700 (Figure 2b). During graphitization, carbon clusters begin to form columnar channels that prevent the blockage of ion diffusion. Nevertheless, raising the temperature to 800 °C further can constrict the interlayer spacing, obstructing the passage of ions through the graphitic interspace.[12] The Brunauer-Emmett-Teller (BET) N_2 adsorption/desorption isotherms also can confirm that the ratio of micropores and the specific surface area increase from Fe/NC/600 to Fe/NC/800 (Figure 2c). The Raman spectra in Figure 2d exhibit sharper G bands as the samples transition from Fe/NC/600 to Fe/NC/800, accompanied by weaker D3 and D4 peaks. This demonstrates

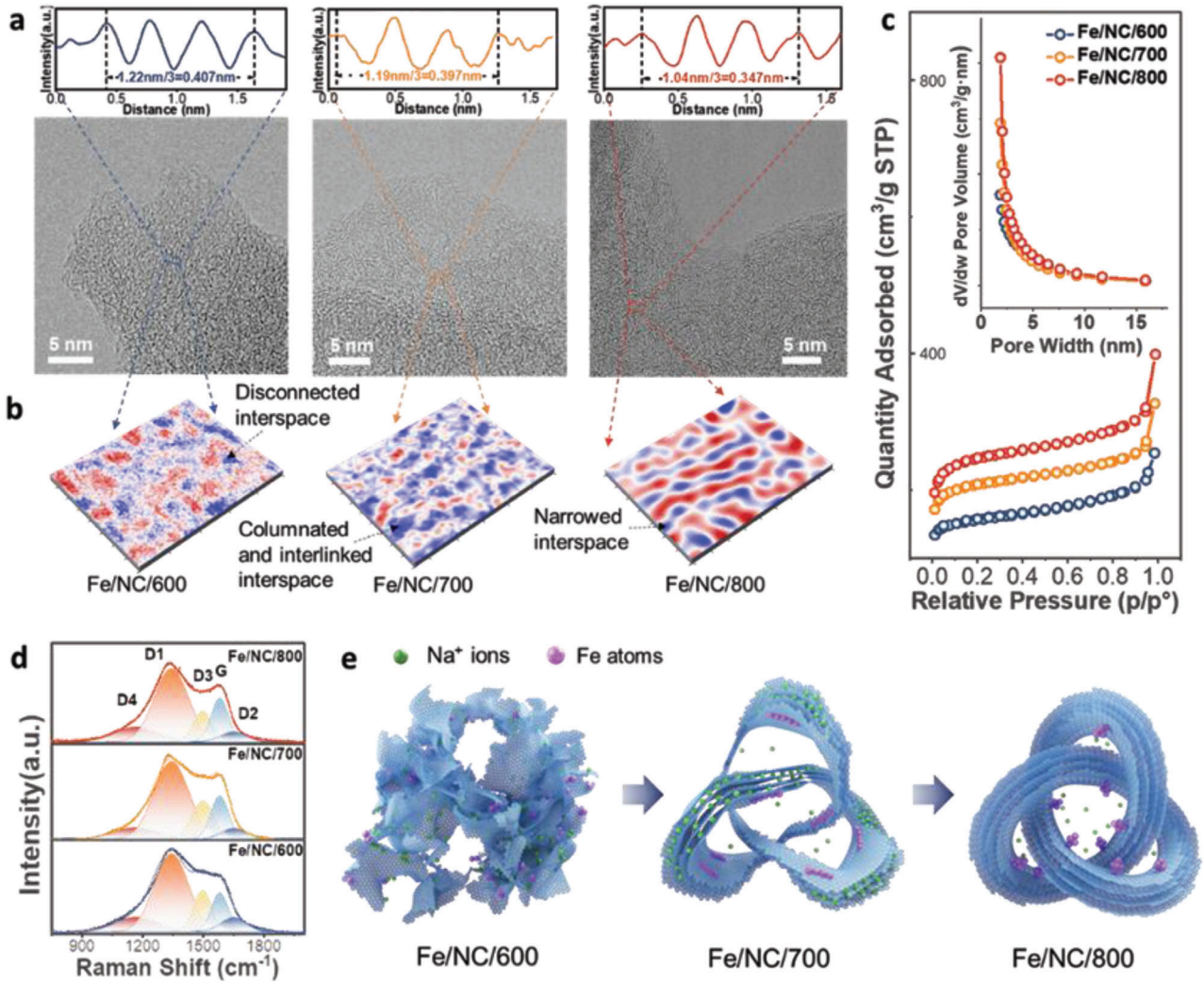

Figure 2. a) STEM images and the crystal spacing of Fe/NC/600, Fe/NC/700, and Fe/NC/800. b) 3D electron intensity profiles of the selected regions in (a). c) BET isotherms and d) Raman spectra of Fe/NC/600, Fe/NC/700 and Fe/NC/800, respectively. e) Schematic illustration of the different ionic channels formed in the Fe/NC/600, Fe/NC/700, and Fe/NC/800, the enlarged channels facilitate the rapid transportation of Na-ions.

an increase in the sp^3 structure of the graphene-terminated edge with increasing temperature. This observation aligns with the XPS results for carbon (Figure S14, Supporting Information). These dynamic changes in the carbon structure finally led to the construction of different topological channels.[13] The high temperature rearranges the unordered carbon islands, resulting in the formation of aligned tubular graphene layers. This transformation process involves the reshaping of the interlayers between different carbon phases, which is crucial for the movement of Na^+ ions and subsequently has an impact on the electrochemical performance. As illustrated in Figure 2e, the Fe/NC/600 configuration likely exhibits an interwoven and disordered carbon structure with intermittent channels. As the temperature increases, the Fe/NC/700 begins to develop partially ordered pseudographitic domains that feature more continuous and wider carbon channels. These channels facilitate the rapid transportation of Na^+ ions. In the Fe/NC/800 configuration, however, where the parallel graphene interlayers become more perfect, the narrow spacing restricts the accessibility of Na^+ ions.[10a,14]

2.2. Electrochemical Performances

To evaluate the electrochemical performance of our samples in Na-S batteries further, sulfur was loaded into all samples (**Figure 3a**). These samples are referred to as S@Fe/NC/600, S@Fe/NC/700, and S@FeNC/800 electrodes. Loaded sulfur is evenly distributed in the three samples (Figures S15–S17, Supporting Information). The thermogravimetric analysis (TGA) results demonstrate a comparable sulfur loading mass of 46 wt% (Figure S18, Supporting Information). The notable reduction in specific surface area implies that the sulfur was completely encapsulated within the pores of all three samples. These samples were then utilized as electrodes and evaluated in coin cells (Figures S19,S20, Supporting Information). Benefiting from the

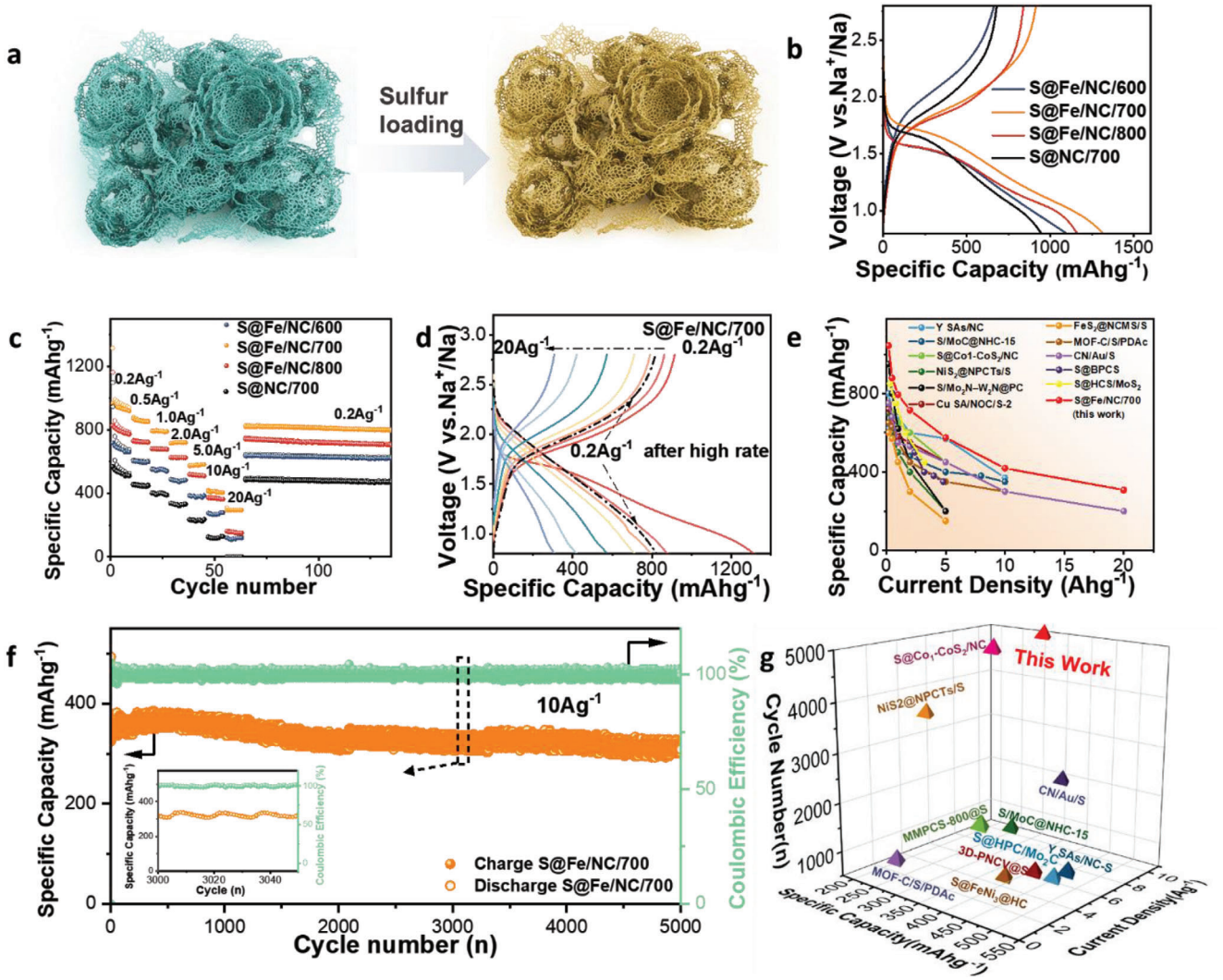

Figure 3. a) Schematic illustration of the S loading process. b) Charge/discharge curves of S@Fe/NC/600, S@Fe/NC/700, S@Fe/NC/800, and S@/NC/700. c) Rate performances of S@Fe/NC/600, S@Fe/NC/700, and S@Fe/NC/800. d) Charge/discharge curves of S@Fe/NC/700 at various current densities. e) Rate performance of S@Fe/NC/700 cell compared to reported counterparts in the literature. f) Long-term cycling stability of the S@Fe/NC/700 at the current density of 10 A g^{-1}. g) Cycling performance of S@Fe/NC/700 compared to reported counterparts.

advanced IFeSACs and ionic channel design, the S@Fe/NC/700 cathode exhibits a highly reversible capacity of 1030 mAh g^{-1} at 0.2 A g^{-1}, surpassing the capabilities of the S@Fe/NC/600, S@Fe/NC/800, and S@NC/700 samples (Figure 3b). This result suggests that the high performance of S@Fe/NC/700 is achieved by the combined effects of the IFeSACs catalyst and the fast ionic carbon channels. Additionally, the S@Fe/NC/700 electrode features a robust cycling life, maintaining a capacity of 825 mAh g^{-1} even after 150 cycles (Figures S21 and S22, Supporting Information).

This demonstrates optimized stability. Furthermore, the capacity of the battery to withstand high rates of charging and discharging is a crucial factor in determining its practicality. Compared to the S@Fe/NC/600 and S@Fe/NC/800 samples, the S@Fe/NC/700 cell exhibits the best reversible capacities of 1030 mAh g^{-1}, 865 mAh g^{-1}, 800 mAh g^{-1}, 735 mAh g^{-1}, 664 mAh g^{-1}, 545 mAh g^{-1}, and 389 mAh g^{-1} at various current densities of 0.2, 0.4, 0.5, 1, 2, 5, 10, and 20A g^{-1}, respectively (Figure 3c). After reverting to 0.2 Ag^{-1}, the S@Fe/NC/700 cell achieves a restored capacity of 860 mAh g^{-1}, with the same charge/discharge curve (Figure 3d). This demonstrates the excellent high-rate performance and highly reversible electrochemical reactions of sulfur and its products when compared to previously reported materials (Figure 3e).[2a,9,15] In particular, the S@Fe/NC/700 cell presents the high reversible capacity of 325 mAh g^{-1} at a large current density of 10 A g^{-1} after 5000 cycles (Figure 3f). And the high coulombic efficiency of 99.99% can be maintained over long cycle. This result also highlights the outstanding high rate cycling stability of S@Fe/NC/700 (Figure 3g; Table S2, Supporting Information). In contrast, the S@Fe/NC/600 and S@Fe/NC/800 show unsatisfactory cycling performances and low reversible capacity at the high current density of 10 A g^{-1} (Figure S23, Supporting Information). Despite a challenging condition with a high sulfur loading of 4–4.5 mg

cm^{-2}, the S@Fe/NC/700 consistently retains an average capacity of 550 mAh g^{-1} at a current density of 1 A g^{-1} throughout 150 cycles (Figure S24, Supporting Information).

2.3. Ultrafast Na^+ Ionic Diffusion Kinetics

The performance of the Na-S battery relies on durable and highly reversible cathodic reactions, which involve efficient electron transport and high ionic conductivity. To reveal the underlying mechanisms of ion migration and electron transfer in these materials, we conducted advanced ex situ and in situ characterizations. First, we collected and analyzed STEM-EDS mappings of the three electrodes after initially discharging them to 0.8 V at a high current density of 10 A g^{-1} to examine the effectiveness of Na^+ transport in the differently constructed carbon hosts (**Figure 4a**). Although uniform distributions of both Na and S were observed in all three samples, the accessibility of Na^+ ions to those hosts differs. As shown in Figure 4b, the Na/S ratio in S@Fe/NC/700 is significantly higher than in S@Fe/NC/600 and S@Fe/NC/800. This indicates that the columnated carbon channels in S@Fe/NC/700 support Na^+ ion transport, leading to an increased efficiency in the S reactions. To eliminate the synergistic effect of the catalyst on the battery performance, we removed sulfur from all three samples and tested their rate performance (Figure S25, Supporting Information). The result indicates that the sample Fe/NC/700 still shows the highest capacity at 10 A g^{-1}, which further verifies that the topological carbon channels in S@Fe/NC/700 can accelerate the Na^+ ion transportation. Besides, the performances of S@NC/600, S@NC/700, and S@NC/800 in Figure S26 (Supporting Information) under a current density of 10 A g^{-1} shows that NC/700 carbon channels still exhibit high performance than other carbon materials. Also, we conducted measurements using the galvanostatic intermittent titration technique (GITT) to analyze the reaction kinetics during the charge and discharge process. This involved discharging the cell at a rate 0.2 A for a period of 30 min, followed by a 3-h relaxation period (Figure 4c; Figure S27, Supporting Information). The diffusion coefficient during reversible charging and discharging can be calculated from the transient voltage response using an expression developed by Weppner and Huggins for the ion diffusion processes in batteries.[16] The analysis revealed that the Na^+ diffusivity of S@Fe/NC/700 is higher than those of S@Fe/NC/600 and S@Fe/NC/800, particularly at a voltage of ≈1.2 V. The fast Na^+ kinetics at this stage can accelerate the liquid-solid conversion of Na_2S_3 into Na_2S_2 and Na_2S, leading to a more complete reaction in sodium-sulfur batteries. We sought to determine the respective contributions of intercalation and capacitive reactions in Na storage by analyzing the Cyclic voltammetry (CV) data at scan rates ranging from 0.1 to 2 mV s^{-1} using the power-law relationship as follows:

$$i = av^b \tag{1}$$

where i is the current (A), v is the scan rate (mV s^{-1}), and a and b are adjustable values. A b-value of 0.5 generally indicates a diffusion-controlled intercalation, while a value of 1.0 indicates that the reaction is surface-limited.[17] The b values of S@Fe/NC/700, S@Fe/NC/600, and S@Fe/NC/800 were all estimated to be 0.8, indicative of diffusion-controlled reactions (Figure S28, Supporting Information). To quantitatively separate the contributions of surface-limited capacitive and diffusion-controlled intercalation components, we used the method proposed by Dunn et al.[18] Based on the dependence between the peak currents and scan rates, we can estimate the contributions of the capacitive and intercalation components by using the following equation:

$$i = k_1 v + k_2 v^{1/2} \tag{2}$$

where i is the current (A) at a given potential, v is the scan rate (mVs^{-1}), and k_1 and k_2 are constants. Here, $k_1 v$ and $k_2 v^{1/2}$ represent the capacitive and diffusion-controlled intercalation components, respectively. Based on Equation 2, the quantitative analysis reveals that S@Fe/NC/700 exhibits a 65% intercalation diffusion. Additionally, it suggests that Na^+ is stored through intercalation at ≈1.2 V (Figure 4d). Therefore, we believe that the topological carbon channels enable the super-fast kinetics of Na^+. Furthermore, in situ high-energy powder diffraction (λ = 0.6885 Å) was utilized to monitor the theta shift of the carbon peak of the sample S@Fe/NC/700 during the charge and discharge process (Figure 4e). After discharge, the carbon peak of S@Fe/NC/700 shifted to the left by 0.2°, and then shifted to the right during charging. The carbon peaks of S@Fe/NC/600 and S@Fe/NC/800, however, show no θ shift or a slight shift after discharge (Figure 4f; Figure S29, Supporting Information). We believe that this is caused by Na^+ rapid intercalation/deintercalation in the process of discharge/charge. This result also confirms that the desired carbon channels in S@Fe/NC/700 are more sufficient for the passage of Na^+ ions, which is crucial to achieve a high-rate battery performance.

2.4. Catalytic Mechanism of IFeSACs

In addition to fast ion conductivity, lowering the energy barrier for reactions and adsorbing the metastable products to prevent dissolution are equally important factors for achieving excellent Na-S performance. The Fe atomic chain plays a vital role in these properties. As shown in **Figure 5a**, the ex situ Fe K-edge XANES spectra of sample S@Fe/NC/700 indicate a redshift to higher energy during the discharge from open circuit voltage to 1.1 V. The result suggests that Fe gradually loses electrons and increases its valence state. While charging to 2.2 V, the S@Fe/NC/700 shifts to a lower energy area. The variations in the valence state of Fe suggest that IFeSACs can interact strongly with sulfur or its polysulfide products. Specifically, IFeSACs donates its electrons to the sulfur cathode during discharge and receives electrons back during the charging process. In addition, the ex situ EXAFS spectra of S@Fe/NC/700 do not show any significant change in the major Fe-N peak, indicating the stable coordination environment of IFeSACs with the carbon host (Figure 5b). The wavelet-transform (WT) results, however, suggest that the intensity maxima near 6.0 $Å^{-1}$ of S@Fe/NC/700 shifts to the left during the discharge process and then returns to 6.0 $Å^{-1}$ after charging (Figure 5c). This implies that the IFeSACs are oxidized from metallic status during the discharge while going back to metallic after the charging process. The reason is possibly because of the donation of

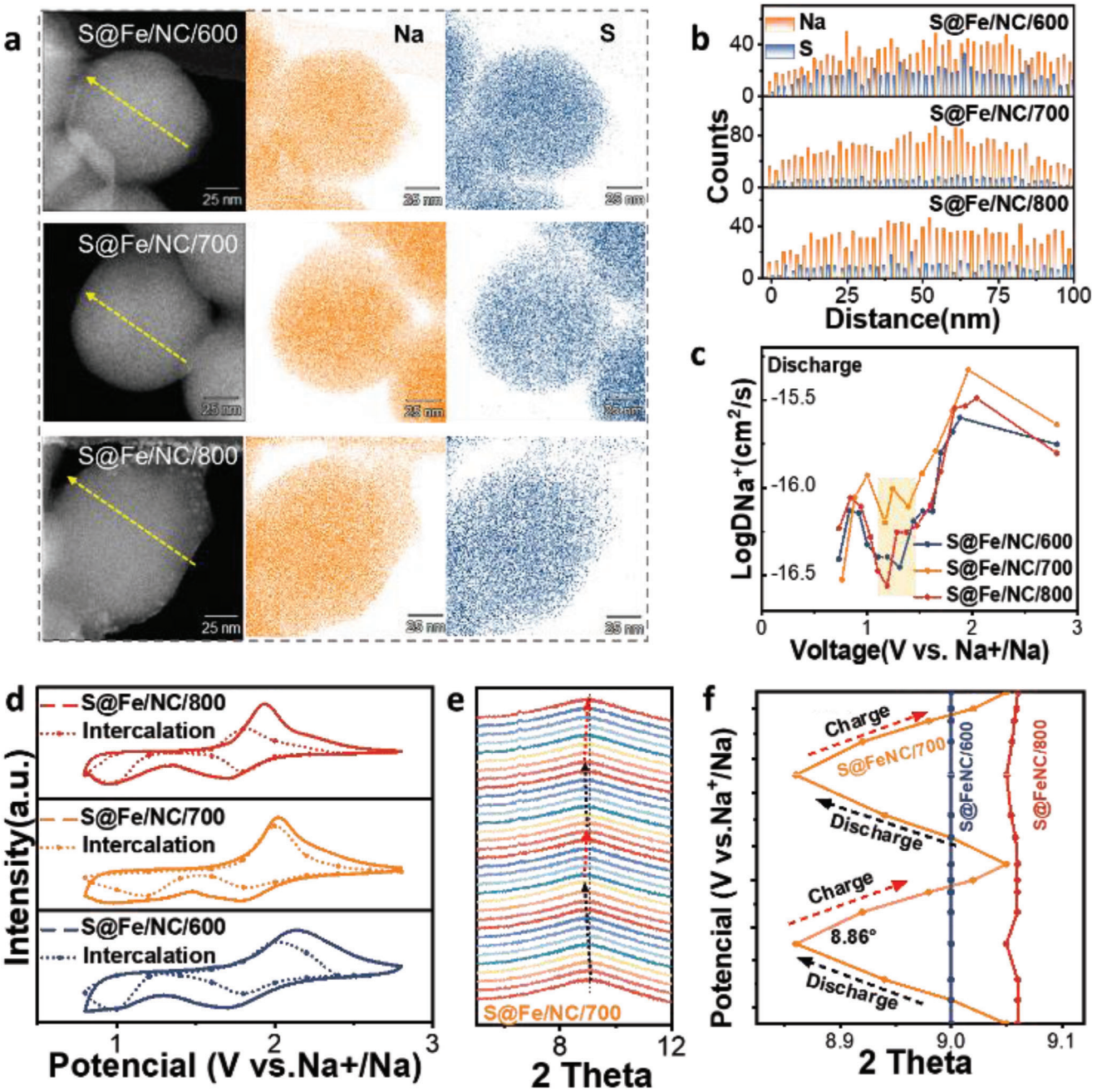

Figure 4. a) STEM-EDS mapping profiles of S@Fe/NC/600, S@Fe/NC/700, and S@Fe/NC/800 particles after the first discharge. b) The Na and S element distributions of S@Fe/NC/600, S@Fe/NC/700, and S@Fe/NC/800 particles as indicated by the yellow arrows in Figure 4a. c) Diffusion coefficients derived from the GITT curves of S@Fe/NC/600, S@Fe/NC/700, and S@Fe/NC/800. d) Voltammetric response for S@Fe/NC/600, S@Fe/NC/700, and S@Fe/NC/800 with a scan rate of 0.2 mV s^{-1}. The total current (solid line) is obtained experimentally, the calculated currents (dotted lines) are determined from cathodic voltammetric sweep data. e) In situ synchrotron XRD patterns of S@Fe/NC/700. f) The carbon peak variations of S@Fe/NC/600, S@Fe/NC/700, and S@Fe/NC/800.

electrons from IFeSACs to sulfur cathode. The electron transfer phenomenon of IFeSACs serves as an efficient electron reservoir, which accelerates the redox reactions of S cathode. As shown in Figure 5d, the S is catalyzed to Na_2S_5 (PDF #: 04-003-2049), followed by Na_2S_3 (PDF #: 00-044-0822) and Na_2S (PDF #: 00-047-0178). What is more important, the Na_2S contributes the major share of the capacity of the discharge process, highlighting the effective catalyzing performance of IFeSACs. This step minimizes the production of highly metastable polysulfide products. It is evident that the outstanding catalytic performance of IFeSACs enhances the conversion between sodium sulfide and sodium polysulfides (Na_2S_5) via electron transfer, enabling a stable reversible reaction during battery cycling (Figure 5e). S@Fe/NC/600 and S@Fe/NC/800, however, show a reduced capacity contribution

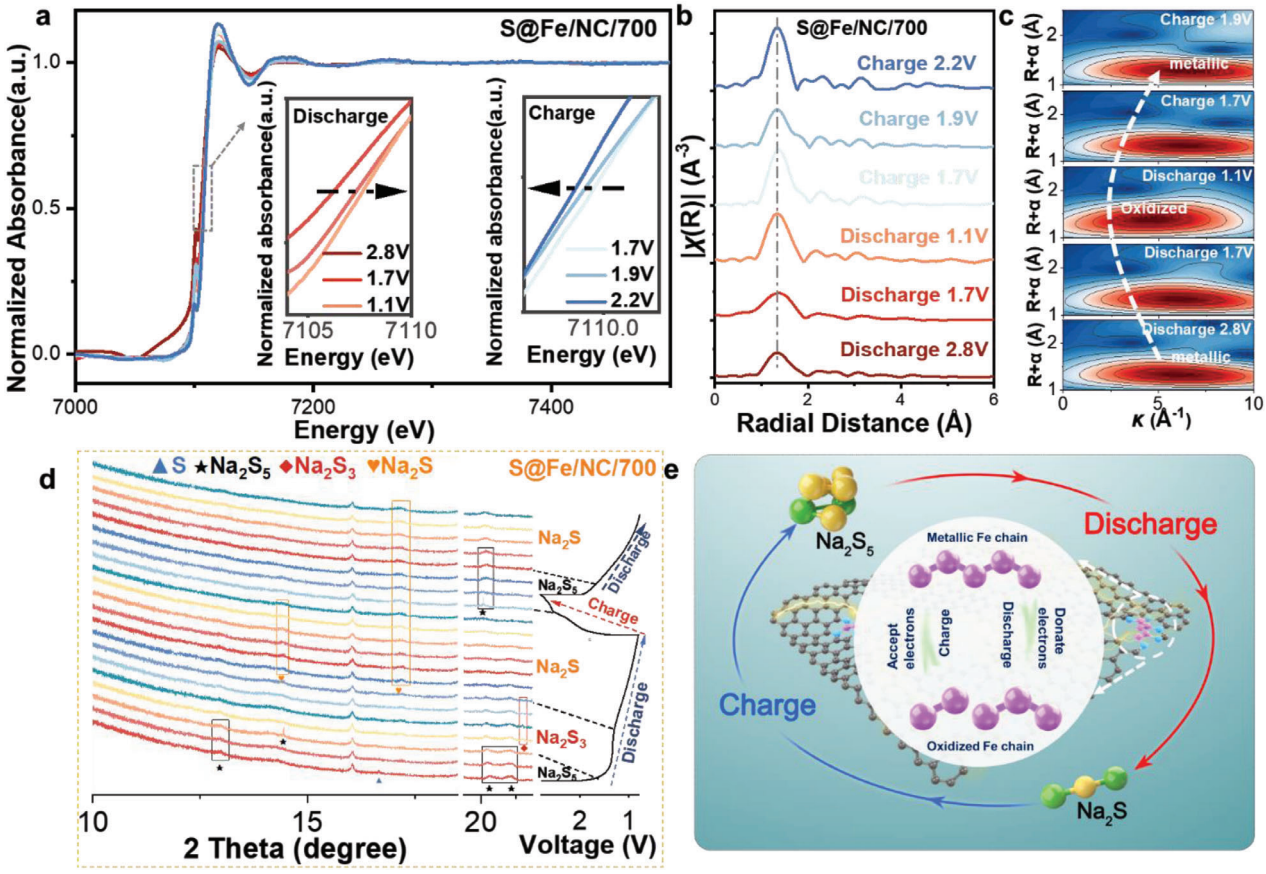

Figure 5. a) Ex situ Fe K-edge XANES spectra of the S@Fe/NC/700 sample during the first discharge and charge processes, with the insets enlargements of the white-line shifts. b) The corresponding ex situ Fe K-edge EXAFS spectra and c) WT plots of the S@Fe/NC/700 sample by using k^3 space. d) In situ high-energy X-ray diffractionXRD patterns of S@Fe/NC/700. e) Mechanism diagram for S@Fe/NC/700 during charging and discharging processes.

from the sluggish Na_2S phase due to their low electrocatalytic efficiency in the solid-solid transition (Figures S30 and S31, Supporting Information). Catalysts with different electronic structures have unique characteristics that affect their electron donation ability. IFeSACs form more metallic bonds, meaning their energy status is closer to the Fe particles compared to Fe single atoms. As a result, IFeSACs have a stronger capability to transfer their electrons to sulfur species due to the large potential differences. This increased ability of electrons filling the antibonding orbital facilitates S molecule cleavage and increase the product selectivity for short chain NaPSs[19] (Figure S32, Supporting Information).

CV tests were performed on S@Fe/NC/700, S@Fe/NC/600, and S@Fe/NC/800 to demonstrate the distinct redox pathways better. According to Figure S33 (Supporting Information), the CV curves for S@Fe/NC/600 show a single redox peak at 1.4 V. The CV curves for the S@Fe/NC/700 and S@Fe/NC/800 electrodes, however, exhibit two broadened peaks during the initial cathodic scan. This suggests that the incomplete conversion of sulfur might be responsible for the observed low first discharge capacity in S@Fe/NC/600, which is consistent with the in situ XRD results.

Another benefit of IFeSACs is its ability to immobilize metastable polysulfides. To demonstrate this, various analysis techniques, including time-of-flight secondary ion mass spectrometry (ToF-SIMS) and XPS depth profiling, have been conducted. First, we conducted ToF-SIMS tests for the S@Fe/NC/600, S@Fe/NC/700, and S@Fe/NC/800, which had undergone 100 cycles (**Figure 6a**). Our results indicate that the content of S^{y-} for all three samples is low on the surface due to the utilization of surface sulfide species in the formation of the cathode-electrolyte interphase (Figure 6b).[20] Interestingly, the S@Fe/NC/700 electrode uses the least time of 632 s to increase its sulfur intensity to 75%. This suggests that the S@Fe/NC/700 electrode has the minimum S loss, indicating the effective inhibition of the dissolution of metastable long chain polysulfides. In addition, the Na^+ intensity in the depth profile of the S@Fe/NC/700 electrode remained high compared to the other two samples. This phenomenon also demonstrates the fast ion kinetics of the topological carbon channels, which is consistent with the EDS results. The Raman spectra also show that the carbon peak remained unchanged after cycling, indicating its structural stability (Figure S34, Supporting Information). These findings provide further evidence that S@Fe/NC/700 is a promising cathode material for Na-ion batteries. To probe the cross-sectional chemical composition, XPS depth profiling was conducted on the cathodes after 100 discharge/charge cycles. The XPS depth profiling (etching under Ar^+ beam for different

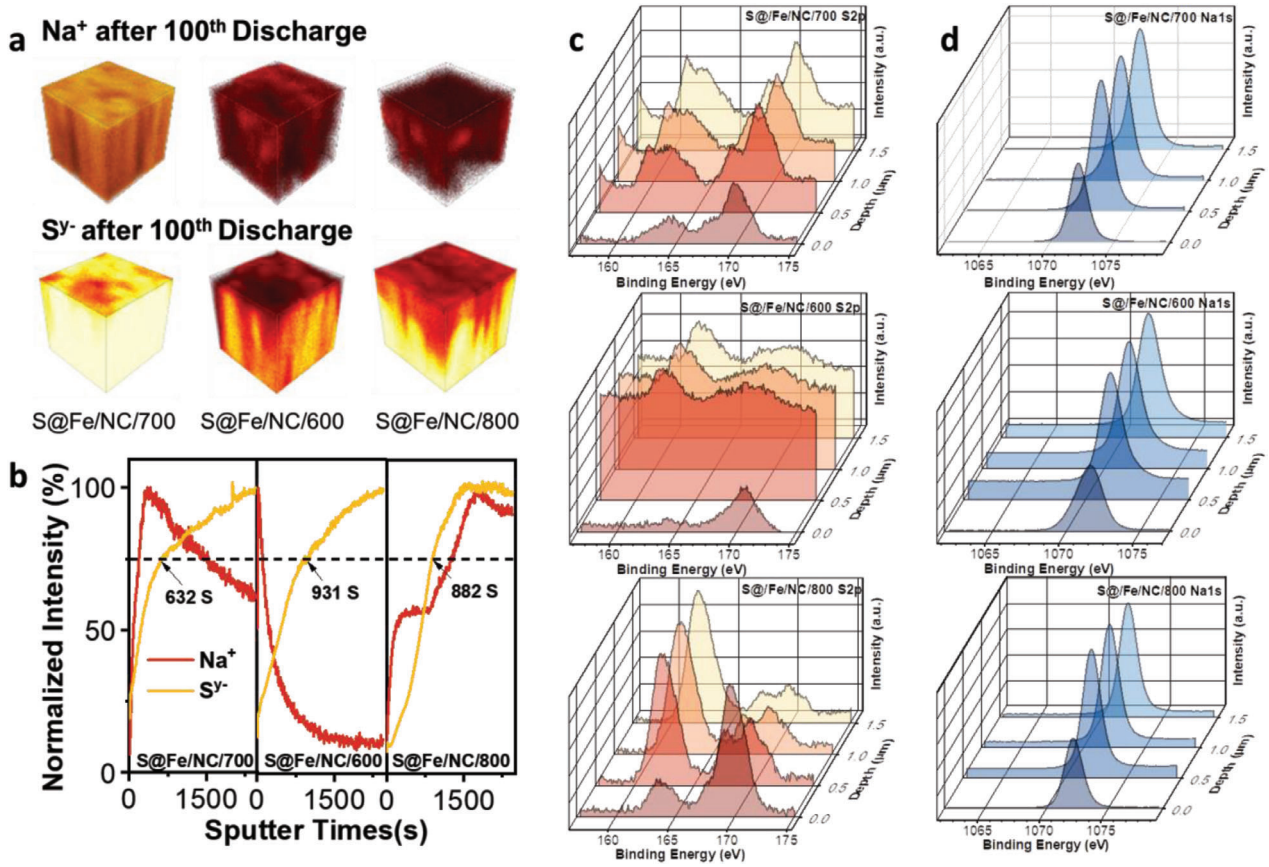

Figure 6. a) 3D reconstructed images of TOF-SIMS depth profiles of Na^+ and S^{y-} after the 100th cycle. b) Normalized depth profiles of secondary ion fragments obtained from the S@Fe/NC/600, S@Fe/NC/700, and S@Fe/NC/800 cathodes after the 100th cycle, respectively. Depth profile spectra of S 2p (c) and Na 1s (d) for S@Fe/NC/600, S@Fe/NC/700, and S@Fe/NC/800, respectively.

time spans: 0, 10, 20, and 30 min) suggests that a thickness of 1.5 μm was being explored, based on the etch rate of the interphase (50 nm min^{-1}). As seen in Figure 6c, the very top layer (0 nm) of S@Fe/NC/700 consists of S-S bonds at 163 eV, while S@Fe/NC/600 has no S-S peak, and S@Fe/NC/800 has a small S-S peak area. This indicates that S@Fe/NC/700 has a strong ability to fix polysulfide. The peak strength of the C-SO_x-C bonds of S@Fe/NC/700 at 170 eV barely changes compared to the latter range of 0.5–1.5 μm, indicating the formation of a stable cathode-electrolyte interphase throughout the electrode.[21] In addition, the Na^+ on S@Fe/NC/700 retains a relatively high value after 100 cycles compared with S@Fe/NC/600 and S@Fe/NC/800 (Figure 6d). Besides, EDS mapping and HADDF-STEM images are conducted to estimate the stability of IFeSACs after 100 cycles. The EDS mapping image reveals a uniform distribution of iron and sulfur in the carbon host, without any noticeable aggregation (Figure S35, Supporting Information). Furthermore, the HADDF-STEM image of S@Fe/NC/700 is in good agreement with the pristine image in Figure 1b, which illustrates the homogeneous dispersion of bright Fe dots, affirming the sustainability of the unique IFeSACs catalyst over prolonged cycling.

3. Conclusions

We report the synthesis of effective interlinked Fe single-atom catalysts anchored on columnated and interconnected carbon channels as cathode matrix for high-rate room-temperature Na-S batteries. Compared to Fe single atoms, the IFeSACs demonstrate a stronger capability of transferring electrons to sulfur cathode due to the lower valence of its metallic bonds. The atomic dispersion of Fe chains shows an improved ability to immobilize the instable products produced during the cycling of Na-S batteries. In addition, the interlinked carbon channels enable fast Na^+ diffusion dynamics, thus providing an interior Na-rich environment and fast conversion kinetics in batteries. The combination of ionic carbon channels and IFeSACs allows for a high rate of S conversion efficiency while maintaining excellent cycling stability. Consequently, the cathode could offer a high reversible capacity of 325 mAh g^{-1} at 10 A g^{-1} after 5000 cycles. This study demonstrates the capability of achieving complete Na-ion accessibility and utilizes atomic-chain Fe for rapid S redox reactions. It offers new insights into the enhancement of the S cathode and presents a promising approach for the effective design of other metal–sulfur batteries.

Supporting Information

Supporting Information is available from the Wiley Online Library or from the author.

Acknowledgements

J.F.R. and Y.-J.L. contributed equally to this work. W.H. Lai would like to acknowledge the financial supported by the Australian Research Council (DE220101113, DP220103301, DP230100198, and DP200100365). Z. Yan thanks the support provided by the National Natural Science Foundation of China (22109041). This research used equipment funded by an Australian Research Council (ARC) Linkage, Infrastructure, Equipment and Facilities (LIEF) grant (ARC-LIEF Grant number) located at the UOW Electron Microscopy Centre. A part of this work was carried out at the Powder Diffraction beamline (beamtime: M20117), and the wiggler XAS beamline (12-ID) (beamtime: M20098) at the Australian Synchrotron, under merit programs. The authors are extremely grateful for the operational support of ANSTO staff, especially Dr. Lars Thomsen and Dr. Bruce Cowie, on the synchrotron data collection. The authors also thank Dr. Tania Silver for her critical reading of this work.

Open access publishing facilitated by University of Wollongong, as part of the Wiley - University of Wollongong agreement via the Council of Australian University Librarians.

Conflict of Interest

The authors declare no conflict of interest.

Data Availability Statement

The data that support the findings of this study are available from the corresponding author upon reasonable request.

Keywords

1D catalyst, carbon channels, interlinked single atom, sodium-sulfur batteries

Received: November 15, 2023
Revised: January 27, 2024
Published online: February 19, 2024

[1] a) W. Hua, T. Shang, H. Li, Y. Sun, Y. Guo, J. Xia, C. Geng, Z. Hu, L. Peng, Z. Han, C. Zhang, W. Lv, Y. Wan, *Nat. Catal.* **2023**, *6*, 174; b) F. Xie, Z. Xu, Z. Guo, M.-M. Titirici, *Prog. Energy.* **2020**, *2*, 042002; c) X. Yin, Z. Lu, J. Wang, X. Feng, S. Roy, X. Liu, Y. Yang, Y. Zhao, J. Zhang, *Adv. Mater.* **2022**, *34*, 2109282.

[2] a) X. Zhou, Z. Yu, Y. Yao, Y. Jiang, X. Rui, J. Liu, Y. Yu, *Adv. Mater.* **2022**, *34*, 2200479; b) L. Zeng, J. Zhu, P. K. Chu, L. Huang, J. Wang, G. Zhou, X. F. Yu, *Adv. Mater.* **2022**, *34*, 2204636.

[3] a) L. Peng, Z. Wei, C. Wan, J. Li, Z. Chen, D. Zhu, D. Baumann, H. Liu, C. S. Allen, X. Xu, A. I. Kirkland, I. Shakir, Z. Almutairi, S. Tolbert, B. Dunn, Y. Huang, P. Sautet, X. Duan, *Nat. Catal.* **2020**, *3*, 762; b) W. J. Lv, Z. Huang, Y. X. Yin, H. R. Yao, H. L. Zhu, Y. G. Guo, *ChemNanoMat.* **2019**, *5*, 1253.

[4] a) Y. X. Wang, B. Zhang, W. Lai, Y. Xu, S. L. Chou, H. K. Liu, S. X. Dou, *Adv. Energy Mater.* **2017**, *7*, 1602829; b) Y. X. Wang, W. H. Lai, S. L. Chou, H. K. Liu, S. X. Dou, *Adv. Mater.* **2020**, *32*, 1903952.

[5] a) Y. Lei, C. Wu, X. Lu, W. Hua, S. Li, Y. Liang, H. Liu, W. H. Lai, Q. Gu, X. Cai, N. Wang, Y. X. Wang, S. L. Chou, H. K. Liu, G. Wang, S. X. Dou, *Angew. Chem., Int. Ed.* **2022**, *134*, 202200384; b) Y. Qi, Q.-J. Li, Y. Wu, S.-J. Bao, C. Li, Y. Chen, G. Wang, M. Xu, *Nat. Commun.* **2021**, *12*, 12; c) L. Wang, G. R. Li, S. Liu, X. P. Gao, *Adv. Funct. Mater.* **2021**, *31*, 2010693; d) W. G. Lim, S. Kim, C. Jo, J. Lee, *Angew. Chem., Int. Ed.* **2019**, *58*, 18746; e) Z. Shen, X. Jin, J. Tian, M. Li, Y. Yuan, S. Zhang, S. Fang, X. Fan, W. Xu, H. Lu, J. Lu, H. Zhang, *Nat. Catal.* **2022**, *5*, 555.

[6] a) Y. Zhang, L. Tao, C. Xie, D. Wang, Y. Zou, R. Chen, Y. Wang, C. Jia, S. Wang, *Adv. Mater.* **2020**, *32*, 1905923; b) W. Lee, J. Kim, S. Yun, W. Choi, H. Kim, W.-S. Yoon, *Energy Environ. Sci.* **2020**, *13*, 4406.

[7] B.-W. Zhang, T. Sheng, Y.-D. Liu, Y.-X. Wang, L. Zhang, W.-H. Lai, L. Wang, J. Yang, Q.-F. Gu, S.-L. Chou, H.-K. Liu, S.-X. Dou, *Nat. Commun.* **2018**, *9*, 4082.

[8] a) Z. Liang, J. Shen, X. Xu, F. Li, J. Liu, B. Yuan, Y. Yu, M. Zhu, *Adv. Mater.* **2022**, *34*, 2200102; b) W. H. Lai, H. Wang, L. Zheng, Q. Jiang, Z. C. Yan, L. Wang, H. Yoshikawa, D. Matsumura, Q. Sun, Y. X. Wang, Q. Gu, J. Z. Wang, H. K. Liu, S. L. Chou, S. X. Dou, *Angew. Chem., Int. Ed.* **2020**, *59*, 22171; c) Z. Han, S. Zhao, J. Xiao, X. Zhong, J. Sheng, W. Lv, Q. Zhang, G. Zhou, H. M. Cheng, *Adv. Mater.* **2021**, *33*, 2105947.

[9] C. Wu, Y. Lei, L. Simonelli, D. Tonti, A. Black, X. Lu, W. H. Lai, X. Cai, Y. X. Wang, Q. Gu, S. L. Chou, H. K. Liu, G. Wang, S. X. Dou, *Adv. Mater.* **2022**, *34*, 2108363.

[10] a) X. X. He, W. H. Lai, Y. Liang, J. H. Zhao, Z. Yang, J. Peng, X. H. Liu, Y. X. Wang, Y. Qiao, L. Li, *Adv. Mater.* **2023**, *35*, 2302613; b) I. Ion, A. Bondar, Y. Kovalev, C. Banciu, I. J. J. O. Pasuk, *A. Materials.* **2006**, *8*, 624.

[11] a) Y. Chen, Z. Li, Y. Zhu, D. Sun, X. Liu, L. Xu, Y. Tang, *Adv. Mater.* **2019**, *31*, 1806312; b) A. Zitolo, V. Goellner, V. Armel, M.-T. Sougrati, T. Mineva, L. Stievano, E. Fonda, F. Jaouen, *Nat. Mater.* **2015**, *14*, 937; c) W. Huang, X. Zhang, J. Chen, Q. Qiu, Y. Kang, K. Pei, S. Zuo, J. Zhang, R. Che, *Adv. Sci.* **2023**, *10*, 2303217.

[12] S. Qiu, L. Xiao, M. L. Sushko, K. S. Han, Y. Shao, M. Yan, X. Liang, L. Mai, J. Feng, Y. Cao, *Adv. Energy Mater.* **2017**, *7*, 1700403.

[13] a) Y. Chen, Y. Xie, X. Yan, M. L. Cohen, S. Zhang, *Phys. Rep.* **2020**, *868*, 1; b) X. Wang, Y. Jia, X. Mao, L. Zhang, D. Liu, L. Song, X. Yan, J. Chen, D. Yang, J. Zhou, K. Wang, A. Du, X. Yao, *Chem.* **2020**, *6*, 2009.

[14] N. Sun, Z. Guan, Y. Liu, Y. Cao, Q. Zhu, H. Liu, Z. Wang, P. Zhang, B. Xu, *Adv. Energy Mater.* **2019**, *9*, 1901351.

[15] a) E. Zhang, X. Hu, L. Meng, M. Qiu, J. Chen, Y. Liu, G. Liu, Z. Zhuang, X. Zheng, L. Zheng, Y. Wang, W. Tang, Z. Lu, J. Zhang, Z. Wen, D. Wang, Y. Li, *J. Am. Chem. Soc.* **2022**, *144*, 18995; b) J. Mou, Y. Li, L. Ou, J. J. E. S. M. Huang, **2022**, *52*, 111; c) Y. Jiang, Z. Yu, X. Zhou, X. Cheng, H. Huang, F. Liu, H. Yang, Y. Yao, X. Rui, Y. Yu, *Adv. Mater.* **2022**, *35*, 2208873; d) Z. Yan, J. Xiao, W. Lai, L. Wang, F. Gebert, Y. Wang, Q. Gu, H. Liu, S.-L. Chou, H. Liu, S.-X. Dou, *Nat. Commun.* **2019**, *10*, 4793; e) S. Zhang, Y. Yao, X. Jiao, M. Ma, H. Huang, X. Zhou, L. Wang, J. Bai, Y. Yu, *Adv. Mater.* **2021**, *33*, 2103846; f) F. Xiao, H. Wang, J. Xu, W. Yang, X. Yang, D. Y. W. Yu, A. L. Rogach, *Adv. Energy Mater.* **2021**, *11*, 2100989; g) L. Wang, H. Wang, S. Zhang, N. Ren, Y. Wu, L. Wu, X. Zhou, Y. Yao, X. Wu, Y. Yu, *ACS Nano.* **2021**, *15*, 15218; h) Z. Yan, Y. Liang, J. Xiao, W. Lai, W. Wang, Q. Xia, Y. Wang, Q. Gu, H. Lu, S. L. Chou, Y. Liu, H. Liu, S. X. Dou, *Adv. Mater.* **2020**, *32*, 1906700; i) F. Xiao, X. Yang, H. Wang, J. Xu, Y. Liu, D. Y. W. Yu, A. L. Rogach, *Adv. Energy Mater.* **2020**, *10*, 2000931; j) J. Dai, Y. Zhu, H. A. Tahini, Q. Lin, Y. Chen, D. Guan, C. Zhou, Z. Hu, H.-J. Lin, T.-S. Chan, C.-T. Chen, S. C. Smith, H. Wang, W. Zhou, Z. Shao, *Nat. Commun.* **2020**, *11*, 5657; k) M. K. Aslam, I. D. Seymour, N. Katyal, S. Li, T. Yang, S.-J. Bao, G. Henkelman, M. Xu, *Nat. Commun.* **2020**, *11*, 5242; l) T. Yang, B. Guo, W. Du, M. K. Aslam, M. Tao, W. Zhong, Y. Chen, S. J. Bao, X. Zhang, M. Xu, *Adv. Sci.* **2019**, *6*, 1901557; m) Q. Lu, X. Wang, J. Cao, C. Chen, K. Chen, Z. Zhao, Z. Niu, J. J. E. S. M. Chen, **2017**, *8*, 77.

[16] W. Weppner, R. A. Huggins, *J. Electrochem. Soc.* **1977**, *124*, 1569.

[17] S. Wei, S. Xu, A. Agrawral, S. Choudhury, Y. Lu, Z. Tu, L. Ma, L. A. Archer, *Nat. Commun.* **2016**, *7*, 11722.
[18] X. Xiao, X. Duan, Z. Song, X. Deng, W. Deng, H. Hou, R. Zheng, G. Zou, X. Ji, *Adv. Funct. Mater.* **2022**, *32*, 2110476.
[19] a) S. Joo, K. Kim, O. Kwon, J. Oh, H. J. Kim, L. Zhang, J. Zhou, J. Q. Wang, H. Y. Jeong, J. W. Han, *Angew. Chem., Int. Ed.* **2021**, *60*, 15912; b) J. K. Nørskov, F. Abild-Pedersen, F. Studt, T. Bligaard, *Proc. Natl. Acad. Sci. U. S. A.* **2011**, *108*, 937.
[20] a) Y. Xu, Y. Wen, Y. Zhu, K. Gaskell, K. A. Cychosz, B. Eichhorn, K. Xu, C. Wang, *Adv. Funct. Mater.* **2015**, *25*, 4312; b) C. Huang, J. Xiao, Y. Shao, J. Zheng, W. D. Bennett, D. Lu, L. V. Saraf, M. Engelhard, L. Ji, J. Zhang, X. Li, G. L. Graff, J. Liu, *Nat. Commun.* **2014**, *5*, 3015; c) H. Pan, J. Chen, R. Cao, V. Murugesan, N. N. Rajput, K. S. Han, K. Persson, L. Estevez, M. H. Engelhard, J.-G. Zhang, K. T. Mueller, Y. Cui, Y. Shao, J. Liu, *Nat. Energy* **2017**, *2*, 813.
[21] a) J. Zhang, M. Zhang, Y. Zeng, J. Chen, L. Qiu, H. Zhou, C. Sun, Y. Yu, C. Zhu, Z. Zhu, *Small* **2019**, *15*, 1900307; b) Y. Li, Y. Ji, Y. Zhao, J. Chen, S. Zheng, X. Sang, B. Yang, Z. Li, L. Lei, Z. Wen, X. Feng, Y. Hou, *Adv. Mater.* **2022**, *34*, 2202240; c) S. Hu, T. Wang, B. Lu, D. Wu, H. Wang, X. Liu, J. Zhang, *Adv. Mater.* **2022**, *34*, 2204147.